

Optogenetic stimulation probes with single-neuron resolution based on organic LEDs monolithically integrated on CMOS

Received: 17 May 2022

Accepted: 13 July 2023

Published online: 17 August 2023

 Check for updates

Adriaan J. Taal^{1,6}, Ilke Uguz^{1,6}, Sabina Hillebrandt^{2,3,6}, Chang-Ki Moon^{2,3,6}, Victoria Andino-Pavlovsky¹, Jaebin Choi^{1,4}, Changmin Keum³, Karl Deisseroth⁵, Malte C. Gather^{2,3}✉ & Kenneth L. Shepard¹✉

The use of optogenetic stimulation to evoke neuronal activity in targeted neural populations—enabled by opsins with fast kinetics, high sensitivity and cell-type and subcellular specificity—is a powerful tool in neuroscience. However, to interface with the opsins, deep-brain light delivery systems are required that match the scale of the spatial and temporal control offered by the molecular actuators. Here we show that organic light-emitting diodes can be combined with complementary metal–oxide–semiconductor technology to create bright, actively multiplexed emissive elements. We create implantable shanks in which 1,024 individually addressable organic light-emitting diode pixels with a 24.5 μm pitch are integrated with active complementary metal–oxide–semiconductor drive and control circuitry. This integration is enabled by controlled electrode conditioning, monolithic deposition of the organic light-emitting diodes and optimized thin-film encapsulation. The resulting probes can be used to access brain regions as deep as 5 mm and selectively activate individual neurons with millisecond-level precision in mice.

Large-scale recording and stimulation of neuronal populations is key to the detection of the underlying behaviour of neural circuitries and their selective manipulation^{1,2}. Current approaches to achieve this are primarily electrical or optical. In the electrophysiological modality, the use of integrated circuits based on complementary metal–oxide–semiconductor (CMOS) technology has led to the microfabrication of implanted electrode arrays with active sites scaled to match the neural networks in their proximity^{3,4}. However, despite the excellent spatiotemporal resolution of these tools for neural recordings, electrical stimulation lacks cell-type specificity and leads to high sparsity⁵. In contrast, for optical techniques, cell-type-targeted promoters can be used to introduce opsins⁶. However, the targeted stimulation of opsin-expressing neuronal ensembles necessitates light delivery systems that provide large fields of view and maintain single-cell spatial and submillisecond temporal resolution.

Methods for light delivery typically rely on the refinement of microscopy techniques, including the use of spatial light modulators⁷. This superficial light delivery can be extended to the deep brain with graded-index lenses⁸ or optical fibres⁹. Illumination typically occurs only within the optical plane near the tip of the endoscope with considerable tissue damage because of diameters in the range of 0.3–1.0 mm. Devices based on integrated photonics to multiplex or shape light delivery are often equally bulky and also require external lasers^{10,11}.

Fully implantable optoelectronic devices that leverage CMOS technology could potentially provide controllable light delivery with large fields of view and minimal displaced tissue volumes. These devices could resemble their electrophysiological counterparts with electronic signalling, converting to light only at the point of transduction to the neural tissue. The face-to-face bonding of gallium nitride (GaN)

¹Columbia University, New York, NY, USA. ²University of Cologne, Cologne, Germany. ³University of St Andrews, St Andrews, UK. ⁴Massachusetts Institute of Technology, Cambridge, MA, USA. ⁵Stanford University, Stanford, CA, USA. ⁶These authors contributed equally: Adriaan J. Taal, Ilke Uguz, Sabina Hillebrandt, Chang-Ki Moon. ✉e-mail: malte.gather@uni-koeln.de; shepard@ee.columbia.edu

micro-light-emitting diodes (μ LEDs) provides more than sufficient optical pulse power (tens to hundreds of milliwatts per square millimetre) and repetition rate for optogenetics^{12,13}. Despite this potential, the mismatch between GaN and silicon prevents the growth of defect-free GaN films directly onto CMOS substrates, thus precluding the monolithic integration of μ LEDs on CMOS¹⁴. Alternative approaches, such as the face-to-face bonding of thinned GaN/InGaN μ LEDs to the CMOS substrate, have low yield and require larger device sizes^{15,16}. Transfer printing via elastomer stamps has been suggested as an alternative route but requires complex fabrication¹⁷. In addition, to achieve fine-tuned emission spectra matched to the excitation spectrum of the opsins, solid-state μ LEDs require either transfer printing from multiple wafers¹⁸ or complex post-processed filter structures¹⁹. As a result, the integration of conventional light-emitting diodes (LEDs) for implantable devices has only been demonstrated in passive structures, in which each LED is hard-wired to its own external contact pad. This leads to a limited number of sources—typically no more than 16 per shank, though up to 144 LEDs was recently reported²⁰—due to wiring limitations, with LED pitches typically constrained to no smaller than 40–50 μm (refs. 13, 21, 22). Given the limited emissive area of μ LEDs and low fill factor, this also limits the integral optical power emitted and the possibility of parallel single-cell stimulation.

Integrated pixels based on organic light-emitting diodes (OLEDs) are a promising technology for the scalable on-chip emission of light. Due to the amorphous structure of organic semiconductor materials used in OLEDs, they can be monolithically integrated on silicon chips and other substrates without any lattice-matching restrictions. The emission spectrum of OLEDs can be tuned across the entire visible spectrum by modifying the emitter material. There have already been substantial research efforts to use OLED-on-silicon technology for microdisplay applications where devices with $>10^6$ individually addressable pixels were demonstrated^{23,24}.

To adapt this technology for use in implantable optoelectronic arrays for optogenetic stimulation, two key innovations were required. First, notably higher optical output powers of 0.1–1.0 mW mm^{-2} or $\sim 5,000$ – $50,000 \text{ cd m}^{-2}$ depending on the wavelength, are needed, compared with the $<0.01 \text{ mW mm}^{-2}$ or $\sim 300 \text{ cd m}^{-2}$ typical for most display applications. Achieving a sufficient output power is challenging with OLEDs, but recent work has demonstrated optical power densities in excess of 1 mW mm^{-2} and robust optogenetic stimulation with OLEDs on glass, flexible substrates and passive silicon substrates using doped charge transport layers, pulsed driving and tandem devices^{25–27}. Second, the devices must be encapsulated in such a way that they can be immersed in aqueous salt solutions without degradation due to the sensitivity of the materials used in OLEDs to water and oxygen. We recently developed a chemical-vapour-deposition-based passivation process for OLEDs that combines an $\text{Al}_2\text{O}_3/\text{ZrO}_2$ nanolaminate with a parylene-based organic coating. This can provide a resilient barrier to water and oxygen and thus facilitate the prolonged exposure of OLEDs to physiological conditions (for example, no loss in function after weeks in a saline buffer and cell culture medium at 37 °C) (refs. 28, 29).

In this Article, we report a monolithically integrated, high-density, large-field-of-view optical probe for neural stimulation. The probe incorporates a total of 1,024 OLEDs with two different colours (orange and blue) and 256 devices on each of the four shanks. The OLEDs measure $21.0 \mu\text{m} \times 19.0 \mu\text{m}$ at a $24.5 \mu\text{m}$ pitch, and satisfy the brightness and repetition rate requirements for the optogenetic stimulation of both red and blue channelrhodopsins. We show that the probe is capable of inducing localized activity at the level of individual pyramidal neurons from a single OLED in mice.

1,024 pixel OLED-on-CMOS neural stimulation probes

Our device is designed on an integrated circuit chip in a 130 nm high-voltage CMOS process. A 2 mm \times 1 mm base contains a decoupling

capacitance and addressing logic. Four shanks, extending 6 mm from the base and at a pitch between shanks of 250 μm , carry two rows of 128 anode drivers each (Fig. 1a). Here 1,024 aluminium pads, each measuring $21.0 \mu\text{m} \times 19.0 \mu\text{m}$ at a $24.5 \mu\text{m}$ pitch, serve as anode contacts for the OLEDs. As the 1-mm-long tip of each shank contains only decoupling capacitance, the furthest anode can be implanted as deep as 5 mm. Each anode contains in-driver logic for local addressing (Fig. 1b). The chip is processed into an implantable-shank form factor with a shank width of 100 μm and a thickness of 55 μm by trenching and back-side milling (Fig. 1c and Methods).

Top-emitting microcavity blue or orange OLEDs are monolithically integrated on these fully packaged probes by high-vacuum, temperature-controlled thermal evaporation of the required stack of organic and metallic films (Methods). A side view of the CMOS and OLED layers is shown in Fig. 1d. The OLED stack on top of the aluminium contact pad consists of a 3-nm-thick silver layer, a 1-nm-thick MoO_3 layer, a p-doped hole transport layer of spiro-TTB:F₆TNAP (190 nm for orange-emitting OLEDs and 150 nm for blue-emitting OLEDs), an electron blocking layer of NPB (10 nm, for orange) or spiro-TTB (10 nm, for blue), an emission layer of NPB doped with the phosphorescent orange emitter Ir(MDQ)₂acac (40 nm) or MADN doped with the fluorescent blue emitter TBPe (20 nm), a hole blocking layer of BAQ (10 nm), an electron transport layer of Cs-doped BPhen (60 nm) and a semitransparent silver top cathode (20 nm) (Fig. 1e). The total thickness of the OLED microcavity is tuned to the second optical maximum for efficiency, forward-directed emission and robustness to substrate roughness (Supplementary Section 1). After OLED integration, the entire device is encapsulated using our recently developed chemical-vapour-deposition-based passivation process that combines $\text{Al}_2\text{O}_3/\text{ZrO}_2$ nanolaminates and parylene layers^{28,29}. The final device structure is visualized by scanning electron microscopy (SEM) after opening up cross sections through the sample with focused ion beam (FIB) milling (Fig. 1f).

OLED characterization

The fabricated probes with 1,024 monolithically integrated OLEDs can be individually addressed through the corresponding anode contact pad. Figure 2a shows a photograph of an orange shank device driven with a chequerboard pattern with 512 OLEDs switched on. Figure 2b shows a blue OLED shank with all the OLEDs turned on (Supplementary Video 1). Supporting electronics control the OLED illumination sequence (Supplementary Section 2).

Figure 2c displays a micrograph of the emission from a single OLED on the shank. The variations observed in light emission over the surface of the electrode are largely the result of surface roughness on the aluminium contacts introduced by the foundry CMOS process (Supplementary Section 3). Because the average surface condition of the anode determines the device performance, micrometre-scale variations in morphology and brightness within individual pixels did not affect the ability of the device to perform targeted optogenetic stimulation. The emission spectra of the blue and orange OLED pixels match the activation spectra of ChR2 and ChRmine, respectively (Fig. 2d).

Figure 2e shows the emitted optical power and forward current as a function of forward voltage for both orange and blue CMOS-integrated OLEDs. Like conventional GaN-based LEDs, OLEDs suffer from a reduction in efficiency at high brightness³⁰ (known as ‘droop’ or ‘roll-off’). Roll-off and ohmic resistance dominate at supply voltages above 5 V, and the measured supply current becomes a linear function of the applied voltage.

Direct integration of OLEDs with CMOS drivers minimizes the parasitic capacitances associated with longer interconnects, which allows us to achieve OLED rise and fall times of 40 and 20 ns, respectively (Fig. 2f). Pulsed operation of the OLEDs at 10 kHz with 50% duty cycle (Methods) is used to reduce degradation from Joule heating and maximize the emission power (Fig. 2g). The ability to support very high pulse

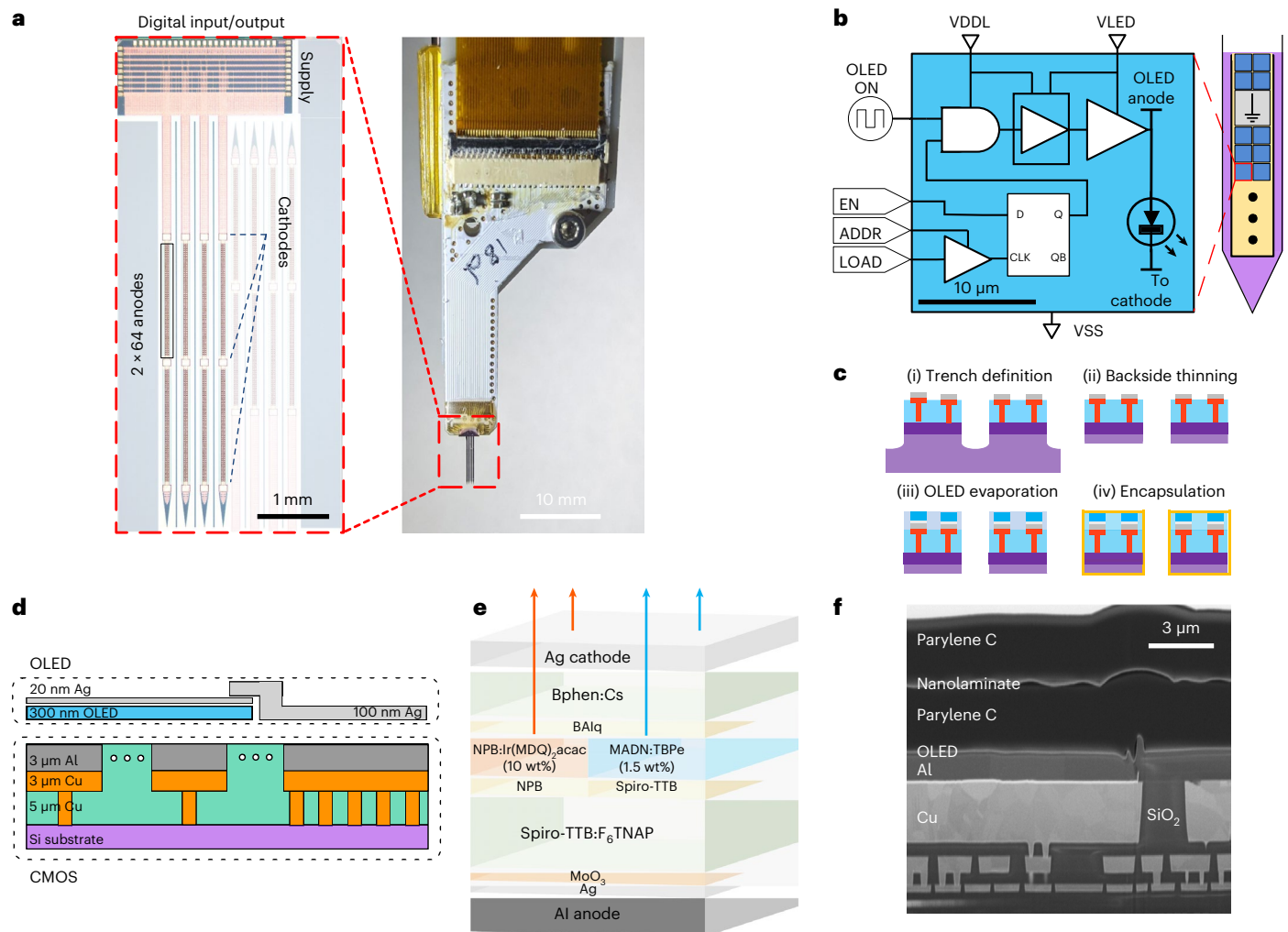


Fig. 1 | OLED-on-CMOS stimulation probe. **a**, Microphotograph of a CMOS die of four-shank probe containing 256 OLED anode drivers and three cathodes per shank. The CMOS chip is bonded to a PCB, which doubles as an insertion guide for neural implantation. **b**, CMOS circuitry is contained underneath each anode pad, and includes local addressing, level shifting and decoupling capacitance. **c**, Fabrication flow from the CMOS die to implantable-probe form factor, with annotated silicon (light purple), active CMOS (dark purple), copper interconnect (orange) and aluminium contacts (grey). Trench definition by laser cutting (i). Back-side thinning removes excess silicon down to 50 μm (ii). Direct evaporation of OLEDs on shanks (iii). Encapsulation with nanolaminate and parylene (iv). **d**, Side-view/cross-section illustration of the CMOS and deposited OLED layers. **e**, Layer architecture of the orange- and blue-emitting OLEDs integrated on the shanks. **f**, SEM/FIB cross section of the completed OLED-on-CMOS stack with aluminium contact pad covering the Cu interconnect, OLED stack and thin-film encapsulation consisting of two pairs of parylene C and oxide nanolaminate.

frequencies creates the opportunity for OLEDs to be carefully matched to the temporal dynamics of any opsin. Under these conditions, the blue OLED pixels emit an average power of 100 nW (0.25 mW mm^{-2}), whereas the orange OLEDs reach an average emitted power of 40 nW (0.10 mW mm^{-2}). These optical powers were measured with the shank in air. Due to the low refractive index of the OLED materials ($n_{\text{OLED}} \approx 1.75$) and thin-film encapsulation ($n_{\text{parylene}} \approx 1.64$), a substantial increase in the efficiency of light extraction from the device is expected when it is in direct contact with aqueous tissue ($n_{\text{tissue}} \approx 1.37$); to a first approximation, this increase is proportional to $(n_{\text{tissue}})^2 \approx 1.9$ -fold.

We perform Monte Carlo simulation in scattering tissue³¹ to predict how much light a neuron receives as a function of distance from the OLED (Methods). The microcavity formed by the electrodes surrounding the organic layers of both blue and orange OLED pixels causes the light to be emitted with an emission profile narrower than Lambertian (Supplementary Section 4). We consider the case of the blue OLEDs, which are assumed to be operating at 7 V—an average optical power density of 0.25 mW mm^{-2} . As shown in Fig. 2h, due to its small size, a single OLED resembles a point source, for which the projected light

falls off quadratically with distance from the OLED. This rapid fall-off in the optical power can be offset by turning on more OLEDs to contribute to the illumination field at the cost of reduced spatial resolution (Fig. 2h). Enabling clusters of contiguous OLEDs increases both volume of stimulation and stimulation intensity.

To induce spikes with 10% probability, ChR2 (H134R) requires an irradiance of approximately 0.1 mW mm^{-2} ; for 100% probability, the power density requirement is 0.5 mW mm^{-2} (refs. 32,33). For the more sensitive redshifted ChRmine opsin^{34,35}, these irradiance requirements are relaxed to $5\text{--}50 \text{ μW mm}^{-2}$ for 10–100% probability. For a single OLED, the ChR2 threshold power densities can only be realized for neurons in immediate proximity to the shank (Fig. 2i); enabling four contiguous OLEDs allows activating neurons stained with ChR2 at a distance of up to 100 μm in the near-threshold regime. However, for ChRmine, this distance can be enhanced to 225 μm by illumination from only a single OLED.

With the maximum supply currents of 35 μA at 7 V and at 10 kHz pulsed operation, the maximum blue OLED power consumption per pixel is 245 μW. For orange OLEDs, the maximum power consumption

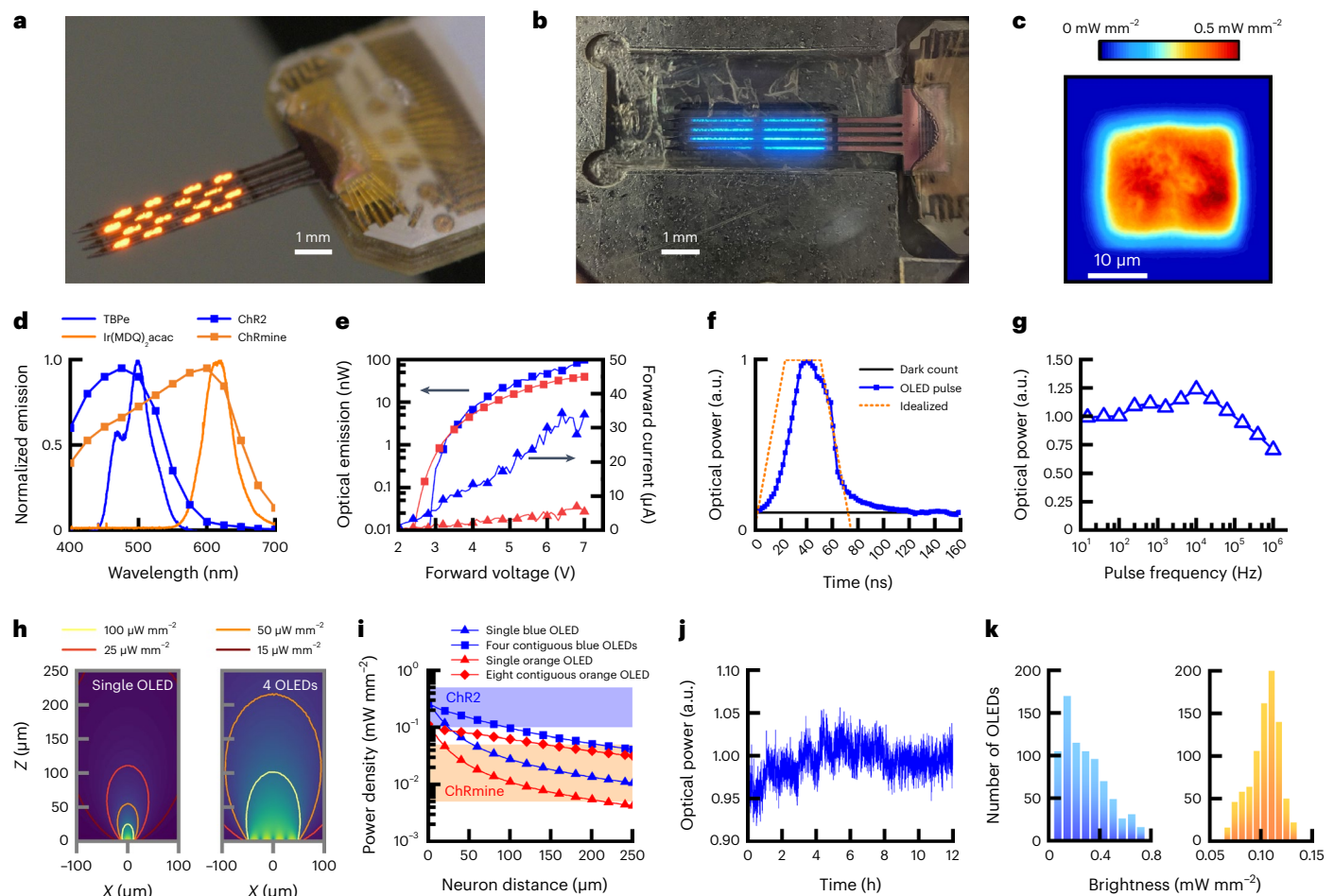


Fig. 2 | Characterization of OLEDs on shank probe. **a**, Photograph of an orange probe with 512 out of the 1,024 OLEDs activated over the four shanks in a chequerboard pattern. **b**, Photograph of a blue probe with all the OLEDs turned on. **c**, False-colour micrograph showing emission intensity over a single OLED pixel on the probe. **d**, Emission spectra for the orange and blue probes are optimized for the channelrhodopsin variants ChRmine and ChR2, respectively. **e**, Emitted power and current as a function of forward voltage for representative orange and blue pixels on CMOS devices. **f**, Temporal evolution of normalized optical power for a blue OLED driven at 6.25 MHz pulsing frequency. **g**, OLED

emission power as a function of pulsing frequency. **h**, Monte Carlo simulation of the optical power projected into scattering neural tissue from a single blue OLED (left) and a cluster of four OLEDs (right) for operation at 7 V. Contours corresponding to different light intensities in the tissue are annotated. **i**, Detailed plot of the projected optical power as a function of distance from the probe for the conditions in **h**. The required optical power densities for ChR2 and ChRmine are annotated. **j**, Stability of OLED emission power over a 12 h stress test. **k**, Histogram of optical power density emitted by blue and orange pixels operated at 7 V forward voltage.

is 49 μW . Comparing these power consumptions with FEM-based simulations of heat dissipation^{36,37} indicates that this results in heating below 1 °C in the tissue surrounding the pixel (Supplementary Section 5). As local heating also leads to the potential degradation of the organic emitter materials, we emulated a long-term neural stimulation experiment by enabling the OLED for repeated cycles in which the OLEDs are on for 5 s (using 10 kHz pulsed operation) and subsequently off for 5 s. Over a 12-h-long stress test, we find no evident degradation (Fig. 2j). The observed variance is instead associated with fluctuations (less than $\pm 5\%$) in the power supply and ambient temperature variations.

To characterize pixel-to-pixel variance, we plot the distribution of the average optical power density generated by each OLED under 7 V pulsed operation (Fig. 2k). For the orange OLEDs, the ensemble is approximately normally distributed with a mean and standard deviation of 0.100 and 0.025 mW mm^{-2} , respectively. We primarily attribute the observed intensity variations to the inhomogeneity of the aluminium anode contacts (Supplementary Section 3), which is negatively impacted by some of the shank post-processing that precedes OLED deposition. The blue OLEDs reach brightness levels of

up to 0.70 mW mm^{-2} but exhibit a mean brightness of 0.25 mW mm^{-2} , thus showing a larger brightness variability than the orange OLEDs (Fig. 2k and Supplementary Section 6). The blue OLED stack is 20% thinner, making the effect of pad inhomogeneity more dominant compared with the orange OLEDs. The performance of OLEDs furthermore strongly depends on the conductivity, reflectivity and work function of their contacts. Any contact resistance on the anode side will affect the blue-emitting device more strongly due to their higher current densities and the higher photon energy of the blue light and the associated higher turn-on voltage.

Large-field-of-view optogenetic stimulation in vivo

To enable electrical recording during optogenetic stimulation, we laminate the OLED-on-CMOS probes on insertion with an optically transparent, mechanically flexible multielectrode array (MEA) (Fig. 3a, Methods and Supplementary Section 7). The noise power spectral density in vivo in the presence of OLEDs pulsing at 10 kHz shows only a minor increase in the integrated noise from 11.9 to 12.8 $\mu\text{V r.m.s.}$ (over the 0.15 Hz to 6 kHz band) (Fig. 3b).

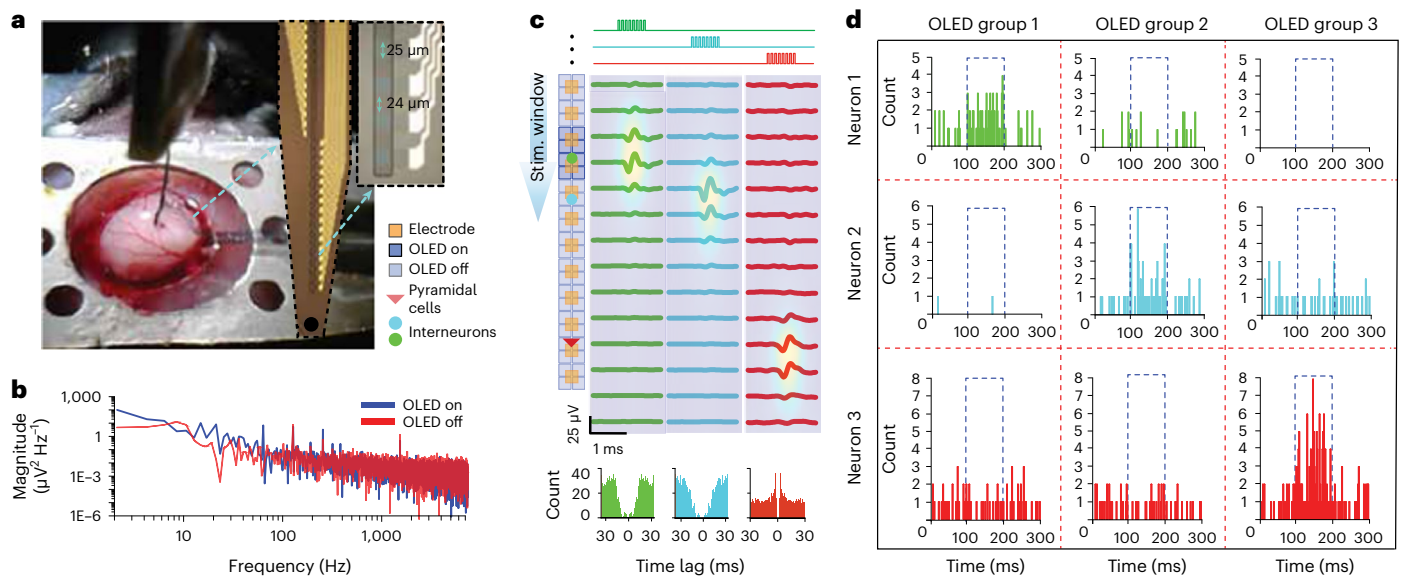


Fig. 3 | Large-scale, hyperlocalized optogenetic stimulation in vivo.

a, Photomicrograph of the neural insertion of a blue OLED shank. Co-implantation of the flexible MEA and rigid blue OLED shank is illustrated. The stimulation probe has the MEA with 32 transparent electrodes at a 49 μm pitch. **b**, Noise spectra of the electrodes before and during blue OLED activation as a function of frequency. **c**, Induced single-unit activity during OLED operation. The left side illustrates the gliding illumination window achieved by the sequential activation of blue OLED groups from the surface to deeper layers. The spike waveforms acquired from electrode sites 3 and 4 show synchronized superficial layer 1 single-unit

interneuron activity (green and cyan circles). In proximity to electrode 10 in layer 2/3, an excitatory pyramidal neuron (red triangle) is synchronously activated to blue OLED pulsing. Detailed waveforms are averaged over 50 spiking events. The corresponding autocorrelograms of each spike is plotted on the bottom part. **d**, Matrix of the firing histogram of each neuron during stimulation pulses applied by each blue OLED group. The dashed blue squares represent the applied stimulation pulses with 100 ms duration. Every pulse is applied for a total count of 100 times. For the corresponding OLED group activation, the responsivity values of neuron 1, neuron 2 and neuron 3 were 63%, 61% and 88%, respectively.

In all of our experiments, a 3 mm \times 3 mm cranial window was created over the somatosensory cortex of a head-fixed anaesthetized mouse using a titanium head plate; the dura mater was removed to minimize the insertion resistance. The recording probe was fabricated to have a through hole located at the tip, whose outer dimension matches the tip of the OLED shank. During insertion, the OLED shank attaches to the flexible recording probe, and they are inserted together as a laminated structure aided by strong hydrophobic interactions. Post-implantation images demonstrate successful alignment with $\pm 8 \mu\text{m}$ precision (Supplementary Section 8). Because the passive electrodes only cover half the OLED shank, the shanks were implanted to a depth of 1.3 mm, providing an interface with 128 OLEDs and 32 electrodes. In all these cases, we operate with 10 kHz pulses, 50% duty cycle and 7 V bias.

We first experiment with transgenic mice expressing ChR2 over the entire cortex³⁸. In this case, to reliably stimulate single neurons with blue OLEDs, we synchronously turn on eight OLEDs, starting from the brain surface and gradually moving towards greater depth. We keep the centre of stimulation over a recording electrode, turning on four OLEDs and turning off four OLEDs to obtain a moving stimulation window. Stimulation is applied for 100 ms at a 3.3 Hz repetition rate for a total of 100 ‘on’ envelope pulses before activating the next group in the moving stimulation window (Supplementary Section 9). In the experiments, we observe a spike success rate of over 60%. Therefore, we choose a minimum of 100 pulses to gather a statistically significant number of spikes.

We extract spike clusters at each electrode and detect the ones that show an increase at the time of OLED stimulation. Figure 3c shows three separate observed spike clusters that exhibit a major increase in spiking frequency during stimulation for at least 50 separate cycles. Two of them are detected at around 150 μm below the surface in layer 2 and show characteristic waveforms and autocorrelograms of interneurons³⁹. The third spike cluster occurs at depths associated with neurons

in layer 5. The fast firing rates and waveform structure of this third detected neuron exhibit the characteristics of a pyramidal neuron³⁹. In every case, spike waveforms recorded by adjacent electrodes show strong attenuation at distances beyond 100 μm . Control experiments performed with wild-type (WT) mice without opsin expression showed a homogeneous spike distribution before and after stimulation onset (Supplementary Section 10).

We observe a substantial increase in synchronized spikes exclusively from the neuron located close to their respective OLED block (Fig. 3d). The fast OLED rise and fall times create the opportunity to study the spike latency, the time from the turning on of the pulse envelope to the peak voltage of the spike. We plotted the histogram of responsive spikes synchronized to the applied stimulation pulse envelopes. For ChR2, we observe a wide range of delays for the observed spikes after the stimulation onset. These variations are consistent with the dynamics of ChR2 at the relatively low illumination power⁴⁰ achieved here, on the order of 0.1 mW mm^{-2} . At these power densities, photon shot noise and ChR2 latency variation contribute notably to spiking temporal uncertainty.

Single-neuron stimulation with high temporal resolution

To further validate the fast switching speed of our OLEDs, we change the opsin model from ChR2 to redshifted ChRmine, which possesses rapid on-kinetics suitable for millisecond-scale control of neural activity⁴¹. In addition, optical modelling indicates that the enhanced sensitivity of ChRmine should allow us to activate neurons with illumination from a single orange OLED (Fig. 2i). To test this, we co-insert the orange OLED shank and recording shanks at a depth of 1.5 mm and activate single OLEDs with 10-ms-long envelope pulses at a repetition rate of 2.5 Hz. Here 200 pulses are applied before moving the excitation window. Figure 4a shows the representative result of one of these experiments in which a pyramidal neuron, adjacent to the emitting OLED, is observed

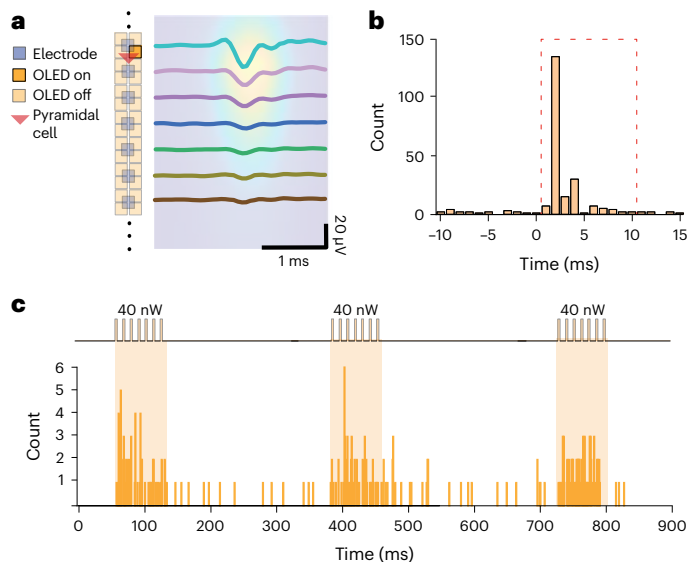


Fig. 4 | Single orange OLED stimulating a single neuron with ChRmine.

a, Spike waveform of the stimulated pyramidal neuron as a function of electrodes placed with $49\ \mu\text{m}$ pitch. **b**, Spiking histogram of the corresponding neuron averaged over 200 pulses with 10 ms width. **c**, Illustration of the firing rate view of the corresponding neuron during a 900 s window. Three separate trains of 200 orange OLED stimulation pulses at 2.5 Hz (illustrated on the top part) are applied for a duration of 80 s each.

to fire synchronous to the stimulation pulses. Supplementary Section 11 provides additional examples with similar kinetics. Over 70% of the corresponding spike distribution (Fig. 4b) is centred within the first 2 ms after the onset of stimulation, band limited by the rise and fall times of the opsin and reflecting the faster kinetics of ChRmine compared with ChR2 (ref. 40). We apply no stimulation pulses for 5 min to let the activity return to the baseline, after which we repeat another 200 stimulation pulses. Figure 4c shows the spike train over 15 min, demonstrating repeatable local spike induction for each successive pulse train.

Modulation of LFPs in vivo

The ability to controllably expand the emission field provides the opportunity for stimulating larger neural populations and modulating local field potentials (LFPs). Here we seek to create a tunable activation window to selectively access groups of neurons by employing simultaneous stimulation from multiple OLEDs and tuning their emission power.

To validate the ability to create reliable and repetitive global stimulation, we first program 128 contiguous OLEDs to apply stimulation cycles consisting of -5 s of illumination followed by -30 s of rest (Fig. 5a). Such illumination timing proved an optimal scheme for reproducible LFP induction, in which the stimulation window is long enough for the further analysis of the frequency components of the induced activity and the delay time is optimal for the excited activity to stabilize to its spontaneous phase post-stimulation (Supplementary Section 12). We record from the flexible, transparent electrodes and establish the periodograms using a Gabor wavelet transform (Methods). We observe a highly reproducible, threefold increase in the corresponding activity, primarily in the 1–25 Hz band, with stimulation that indicates the large-scale modulation of neural activity. To confirm that these effects are due to optical stimulation and not heating from the device, control experiments are performed in mice without opsin expression. The corresponding LFP activity does not show any change during OLED activation (Supplementary Section 13).

Although all the results presented thus far have been for a maximum applied voltage of 7.0 V, the addressable stimulation depth can also be adjusted by tuning the applied OLED anode potential to be

5.5, 6.0 and 7.0 V (Fig. 5b). When illuminating synchronously from 16 contiguous OLEDs, the total optical power emitted by the OLEDs at these three different voltages corresponds to 0.15, 0.35 and 0.65 μW , respectively, which is in direct proportion with the effective field of stimulation (Supplementary Section 14). To be able to precisely validate the controlled LFP modulation, we ensure that the brain is in the same state of sleep before the application of stimulation pulses and that the spectral domains acquired by computing the power spectra of the signals overlap. All the prestimulation spectra exhibit a peak in the 1–2 Hz range, a marker of slow-wave sleep-like activity obtained under deep anaesthesia⁴², and a 7–10 Hz peak characteristic of the somatosensory cortex in this state of anaesthesia. Modulation with 0.15 μW enhances the power spectra between 10 and 40 Hz, largely in the beta band. Increasing the emission power levels to 0.35 and 0.65 μW enhances the LFP modulation over a larger frequency range of 0–40 Hz with power spectra that varies in proportion to the incident optical power density.

For more focused induction of LFPs, we instead apply stimulation pulses only to the top and bottom 16 OLEDs out of a 128 OLED group that is integrated with 16 electrodes spaced at $98\ \mu\text{m}$ pitch. Figure 5c shows the recording from two separate experiments with mice that were injected at depths of 300 μm and 1.2 mm. Induced activity, observable as far as 1.5 mm away from the point of stimulation, is primarily concentrated around the active OLEDs. The corresponding LFP power analysis shows a major decay as a function of distance towards distant electrodes (1.44 mm), which is consistent with the optical stimulation being the input source. These results show that the light emission field can be extended both laterally by expanding the number of OLEDs and axially by increasing the emitted optical power.

Conclusions

Our OLED-on-CMOS design is part of a new class of implantable optoelectronic devices that use CMOS technology to create volumetrically efficient implants for optical brain interfaces. An important requirement, both for optogenetic stimulation and for imaging, is to shape the illumination field both spatially and temporally. OLEDs bring fabrication advantages, and unlike other LED choices, allow emitter density (and pixel pitch) to be pushed to neuron-scale densities. Because the sheet resistance of the OLED layers exceeds $500\ \text{M}\Omega\ \square^{-1}$, the spacing between OLEDs is not limited by lateral conductance⁴³. Instead, the size of each OLED and OLED fill factor is entirely determined by the design rule constraints on the aluminium contact pads of the foundry CMOS process. As a consequence of the active CMOS control, our completed devices can be set to create arbitrary illumination patterns, within the limits of the lateral dimensions of the anode contacts (that is, $24.5\ \mu\text{m}$ in this study).

Using this flexibility, we have demonstrated the ability to stimulate neuron populations at various temporal and spatial scales using different patterns of structured illumination, from individual neurons with single OLEDs to large populations of neurons with synchronized excitation of larger OLED groups. In earlier-generation devices, LEDs were often separated from their driver by significant interconnect networks; in our case, the CMOS drivers are immediately beneath the OLEDs and tuned to drive the OLED capacitance. The resulting fast rise and fall times are well suited for the high-frequency modulation of neuronal activity with opsins offering submillisecond kinetics, such as Chronos⁴⁴ or ChroME2f (ref. 45).

A key advantage of optogenetic stimulation is the possibility of bidirectional stimulation—the activation and inactivation of neuronal activity⁴⁶. Here we have demonstrated two different OLED colours—blue and orange—that overlap with the characteristics of ChR2 and ChRmine. In future work, we expect that the variability can be considerably reduced by changing the driver design to constant current driving. Furthermore, multiple colours can be integrated on the same shank by optimizing the masking process. Very high-resolution (less than $5\ \mu\text{m}$) shadow-masking methods^{47,48} could be used to pattern different colours on the pixel level. This approach would allow the bidirectional

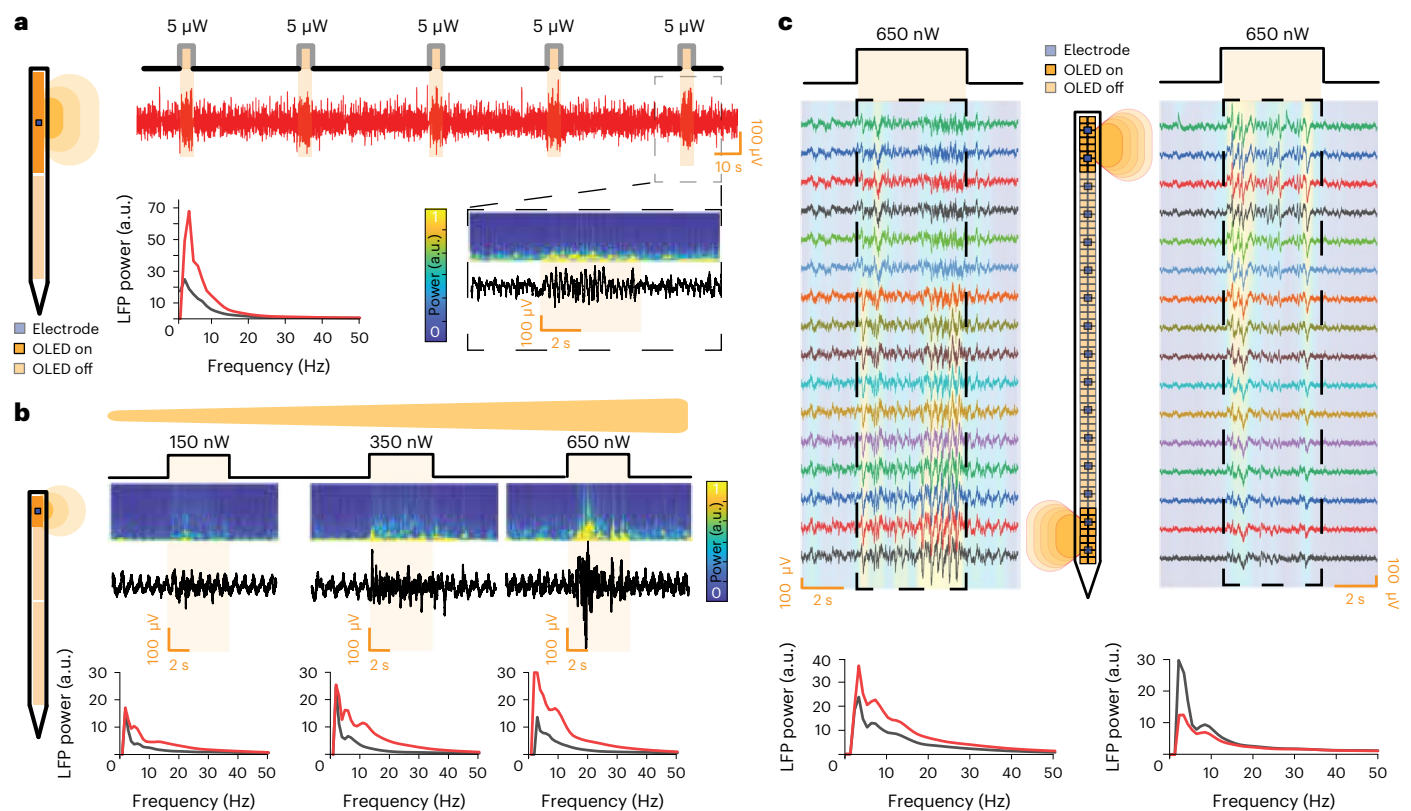


Fig. 5 | LFP modulation in vivo. **a**, LFP modulations in the delta, theta and alpha bands are reproducibly induced by the simultaneous activation of 128 orange OLEDs in ChRmine-injected mice. The square pulses represent the time of applied stimulation. The corresponding time–frequency colour map is placed on the bottom right. LFP power spectra as a function of frequency before (black) and during (red) stimulation within 0–50 Hz range is plotted on the bottom left. **b**, Induced LFP modulations as a function of the applied power emission for 150,

350 and 650 nW. The square pulses represent the time of applied stimulation. The bottom row illustrates the corresponding LFP power spectra as a function of frequency before (black) and during (red) stimulation within the 0–50 Hz range. **c**, LFP modulation fallout as a function of distance from the active OLED groups over a distance of 1,500 μm . The corresponding power spectra are located at the bottom, showing the LFP power at the top electrode (black) and bottom electrode (red).

stimulation of opsins, such as SOUL, with non-overlapping activation and inhibition at orange and blue wavelengths, respectively⁴⁶.

In some of our experiments, we pulsed small groups of OLEDs, successively running the active pixels along the entire length of the shank, which resulted in 3-h-long experiments. In addition, we performed multiple implantations of the same shank in separate animals. In aggregate, shanks were operated and remained functional in vivo for at least 24 h.

Here we have used a second laminated probe to validate the stimulation capabilities of the OLED shank, but these electrodes and the associated recording electronics can be integrated onto the CMOS shank itself. To further increase the addressable volume, the OLED brightness can be further improved through improvements to the planarity and surface resistance of the foundry-provided aluminium pad. Relative to our OLED-on-CMOS structure, OLEDs with optimized electrode contacts deposited on glass or passive silicon substrates have been shown to reach up to tenfold higher brightness levels at the same drive voltage^{27,49}. Finally, although we performed die-level OLED-on-CMOS fabrication here, the process can be scaled to the wafer level if the thermal budgets during dicing and post-processing can be managed to maintain the OLED performance. The wafer-level processing of OLEDs on CMOS has been demonstrated for microdisplays, although with lower-brightness OLEDs^{23,24,50,51}.

Methods

Shank layout and fabrication

The CMOS is designed in a 130 nm process (TSMC). We first define the probe shape by thermally ablating 100- μm -deep and 25- μm -wide

trenches with a Cu-vapour micromachining laser⁵² (IPG Photonics) at a wavelength of 532 nm. This process takes less than 60 s per die and produces side-wall profiles (Supplementary Section 15). The laser uses a repetition rate of 20 kHz and pulse length of 10 μs . The local thermal ablation did not impact the circuitry performance. Using an X-Prep mechanical polisher (Allied High Tech), the devices are thinned to a thickness of 55 μm , releasing the probes from the die, which are then wire bonded to the daughterboard printed circuit board (PCB). The daughterboard carries a connector and decoupling capacitance of 4.7 μF for each of the supply voltage lines. This daughterboard PCB connects to a motherboard to allow data transfer of arbitrarily programmable patterns of OLED illumination at a maximum frame rate of 39,000 frames per second.

An externally provided global LED_{ON} shutter clock allows the OLEDs to be synchronized with electrophysiological recording. Three large cathode pads (80 $\mu\text{m} \times 80 \mu\text{m}$) are located at the base, middle and end of the shank, distributing the OLED forward current. Furthermore, each shank contains a 2×128 array of single-photon avalanche diodes⁵³, providing a future platform for fully integrated fluorescent imaging studies.

External electronics

The daughterboard PCB is connected through a flexible cable to a motherboard, carrying an Opal Kelly XEM6310 and voltage regulators. The Xilinx Spartan 6 field-programmable gate array inside the Opal Kelly contains a state machine that controls the OLED patterning and clocking. Initially, the field-programmable gate array sequentially

cycles through the 1,024 pixel addresses, and asserts the LOAD signal to flash EN into each pixel's local one-bit memory (Fig. 1b). Flashing the 1,024 pixel pattern takes approximately 25 μ s. The global OLED on clock activates all the OLEDs that were enabled in pixel. The pulse frequency, duty cycle and number of pulses before switching to the next pattern are dynamically programmed in the state machine.

OLED fabrication

The reference OLEDs were fabricated on Eagle XG glass substrates with a thickness of 1.1 mm, which were cleaned in ultrasonic baths with acetone and isopropanol. The substrates were dried with nitrogen and subjected to oxygen plasma treatment (3 min).

By postponing OLED deposition onto the CMOS backplane until the end of the fabrication process, the probe can be aggressively cleaned and wire bonded at temperatures of up to 100 °C without risking degradation in OLED performance. To render the anode contacts on the shanks suitable for OLED integration, they were preconditioned via a reactive ion etch plasma process. The reactive ion etch process (Sentech Instruments) was performed at 20 s.c.c.m. CHF₃ flow with 100 W radio frequency and 100 W inductively coupled plasma. The etch rate for aluminium oxide at these parameters was 0.9 Å s⁻¹. After etching for 200 s, the shanks were immersed in 80 °C warm deionized water for 60 s to wash away the top-most AlF formed during the reactive ion etch step. After drying with nitrogen, they were mounted in a custom-made sample holder with precision alignment pins to guide the accurate alignment between the contact pads on the shanks and each of the shadow masks used during deposition.

The OLED deposition was performed in a high-vacuum chamber (Angstrom) via thermal evaporation from temperature-controlled crucibles at a base pressure of $\sim 10^{-7}$ mbar. The deposition rates and thicknesses were monitored by quartz crystal balances. The alignment of each mask was checked and, if needed, adjusted under a microscope inside a nitrogen-inert-gas glovebox. After the deposition of the OLED stack including the 20-nm-thick silver cathode layer on the shank devices (Supplementary Section 16 provides further details), the devices were transferred into a nitrogen-filled glovebox without air exposure to exchange the deposition mask. After the shadow mask for depositing the interconnects from the cathode layer on the OLED stack to the large cathode pads is positioned, the devices were placed back into the deposition chamber for the final deposition step of a 100-nm-thick silver layer. The short lateral diffusion length for minority carriers inside the organic materials ($\ll 3 \mu$ m) electrically isolates each OLED from all the neighbouring OLED pixels and the actual pixel size is, therefore, solely determined by the underlying anode contact on the CMOS chip.

The organic materials used in the OLEDs were 2,2',7,7'-tetra (*N,N*-di-*p*-tolyl)amino-9,9-spirobifluorene (spiro-TTB), 2,2'-(per fluoronaphthalene-2,6-diylidene)dimalononitrile (F₆TNAP), *N,N'*-bis(naphthalen-1-yl)-*N,N'*-bis(phenyl)-benzidine (NPB), bis(2-methyldibenzo-[f,h]quinoxaline)(acetylacetonate)iridium(III) (Ir(MDQ)₂acac), 2-methyl-9,10-bis(naphthalen-2-yl)anthracene (MADN), 2,5,8,11-tetra-*tert*-butylperylene (TBPp), bis(2-methyl-8-quinolinolate)-4-(phenylphenolato)aluminium (BALq) and 4,7-diphenyl-1,10-phenanthroline (BPhen); they were purchased from Lumtec and used without further purification.

Next, the devices were again transferred from the vacuum chamber to the nitrogen-filled glovebox without intermittent exposure to air and then encapsulated/passivated by a combination of atomic layer deposition of the nanolaminates of Al₂O₃ and ZrO₂ and parylene C (diX coating, Kisco), as described elsewhere²⁸. In brief, the layer sequence of the encapsulation was 50 \pm 5 nm nanolaminate, 5 \pm 1 μ m parylene C, 50 \pm 5 nm nanolaminate and 5 \pm 1 μ m parylene C. The nanolaminates and parylene C were deposited using an atomic layer deposition reactor (Savannah S200, Veeco) and a parylene coater (P8, Diener), respectively, with both coaters directly connected to the nitrogen-filled

glovebox. For the nanolaminate, an alternating series of 3-nm-thick sub-layers of Al₂O₃ and ZrO₂ were deposited using either 33 cycles of a 15 ms trimethylaluminum pulse/10 s N₂ purge/15 ms H₂O pulse/10 s N₂ purge or 17 cycles of a 300 ms tetrakis(dimethylamino)zirconium pulse/7 s N₂ purge/30 ms H₂O pulse/7 s N₂ purge. The tetrakis(dimethylamino) zirconium precursor was heated to 75 °C; the trimethylaluminum and H₂O cylinders were maintained at room temperature. The process temperature and base pressure of the atomic layer deposition reactor were 80 °C and 0.1 torr, respectively. The parylene C powder was vapourized at 130–140 °C and the gaseous dimer was pyrolysed into a monomer at 690 °C. The polymeric films of parylene C were then formed on the devices in the main vacuum chamber of the parylene coating system, which was kept at room temperature and at a base pressure of <25 mtorr.

OLED characterization

The characterization of the reference OLEDs was performed as described in another work⁵⁴, measuring the angular emission characteristics with a goniometer and including any deviations from Lambertian characteristics when computing the optical power density.

The emission power of OLEDs deposited on CMOS was measured using an Olympus BX51 microscope. A $\times 50$ 0.8-numerical-aperture objective (Nikon UmPlanFL) collected the OLED light with a maximum angle of 53°. The photon intensity was measured with a Thorlabs CS2100M-USB scientific CMOS camera. The photon counts were calibrated against the output of a multimode fibre (Thorlabs, 0.39 numerical aperture) coupled to a 465 nm LED (Doric) with a bandwidth of 25 nm. The emission of the fibre-coupled LED is measured using a Newport 1936-R power meter with 818-SL-L-FC/DB calibrated photodiode.

OLED operation

Whenever the OLEDs on the CMOS are nominally 'on', we operated them in a fast, pulsed mode at 10 kHz, 50% duty cycle rather than continuously. Due to reduced heating in this operation mode, this increased the total emission power by 25%. Given that this frequency range is far faster than the opsins can respond to, we used an envelope function with a time window in the range of milliseconds for spike induction and in the range of seconds for LFP induction to modulate this high-frequency pulse train. Similar pulsing strategies have been used in two-photon optogenetic stimulation⁵⁵. Fast pulsing was possible because opsins have off-kinetics⁵⁶ on the order of 10 ms and only respond to the average optical power for temporal waveforms faster than this. The peak average emission power reached for a 50% duty cycle at our chosen operating frequency of 10 kHz (Fig. 2f). Beyond 10 kHz, the finite rise and fall times decreased the total output power.

FIB/SEM and AFM characterization

Cross sections for SEM were prepared using FIB milling with a Ga ion source at an accelerating voltage of 30 kV, followed by final polishing at 5 kV (FEI Scios DualBeam).

We measured the contact pad and shank side-wall surface roughness using a Bruker atomic force microscopy (AFM) instrument. After releasing the probes from the CMOS die, we broke off a shank and adhered it flat and sideways to a carrier wafer. The AFM cantilever scanned a 50 μ m \times 50 μ m area.

Optical scattering simulation

We used the ValoMC³¹ finite element modelling package for MATLAB 2021a to simulate optical scattering in tissue. Scattering was modelled with a Henyey–Greenstein distribution, parameterized with anisotropy factor $g = 0.88$, refractive index $n = 1.37$ and scattering and absorption coefficients of $\mu_s = 21.00 \text{ mm}^{-1}$ and $\mu_a = 0.06 \text{ mm}^{-1}$, respectively⁵⁷. This distribution model was shown to follow the experimental values⁵⁸.

Electrode design

The passive electrode array has 32 μm electrodes on a 49 μm pitch; the active area of the recording MEA is constructed from 50-nm-thick PEDOT:PSS electrodes, sandwiched between two parylene layers. The high optical transparency of the PEDOT:PSS films (95%) allows the simultaneous recording of local neuronal activity during optical stimulation; the high capacitance of the PEDOT:PSS electrodes enhances the signal-to-noise ratio for electrical recording. The passive recording array has 32 electrodes in a configuration such that on lamination and on insertion, every four OLEDs have an electrode located in the centre (Fig. 3c). Electrodes were coupled with an Intan RHS recording system for signal acquisition. The system allowed for a range of sampling rates, typically between 300 Hz to 30 kHz, depending on the nature of the recorded signal, whether it was single units or LFPs.

Electrode fabrication

A three-inch silicon wafer was coated by 2 μm of parylene film using chemical vapour deposition by an SCS parylene coater. A 10-nm-thick Ti adhesion layer, followed by a 100-nm-thick Au layer was deposited and patterned using a lift-off process. A PEDOT:PSS dispersion was spin coated on the wafer and baked at 115 °C for 30 min. A layer of PMMA 495 as a protective layer to prevent the exposure of PEDOT:PSS to the developer for subsequent photoresist development step was spin coated at 2,000 r.p.m. and cured at 130 °C for 5 min. A 1 μm film of S1811 was patterned to provide an etch mask for PEDOT:PSS patterning. A dry etch process is performed with plasma reactive ion etching (Oxford Plasmalab 80; 100 W, 30 s.c.c.m. O_2 and 2 s.c.c.m. SF_6) and the residual photoresist is rinsed off using Remover PG. Before coating with the top layer of insulation, a layer of photoresist (S1811, 3,000 r.p.m. for 2 min followed by a soft bake at 110 °C for 2 min) was deposited on PEDOT:PSS to protect it during final etching required to define the recording electrodes. A second layer of parylene was deposited using silane A174 as the adhesion promoter. An 8 μm layer of AZ9260 was patterned as the etch mask. A second dry etch process is performed only over the active electrodes with plasma reactive ion etching (Oxford Plasmalab 80; 180 W, 60 s.c.c.m. O_2 and 2 s.c.c.m. SF_6). Residual S1811 over the electrode area was rinsed off using Remover PG. The contour of the shanks and through holes were patterned using an IPG Photonics excimer laser.

ChRmine injections

AAV-ChRmine (AAVdj-CaMKIIa-ChRmine-Oscarlet-Kv2.1 with a titre of 7.5×10^{11} vg ml^{-1}) was used for injections. The CaMKIIa promoter drives the expression of ChRmine in excitatory neurons in the neocortex and hippocampus. The Kv2.1 peptide tag minimizes the ChRmine expression in axons to maximize the relative somatic expression³⁵.

Six-to-eight-week-old animals (Jackson Laboratory strain #000664) were anaesthetized with 1–5% isoflurane. A 0.25 mm opening was drilled on the skull taking special caution not to puncture the dura (1.5 mm anterior to posterior, 1.5 mm medial to lateral; Bregma). Using a pulled glass pipette as a needle (50 μm tip) and a 10 μl Hamilton syringe mounted on a microsyringe pump (World Precision Instruments, SMARTouch), three 500 nl injections were made into the cortex, at 0.5, 1.0 and 1.5 mm depth. The injection rate was 80 nl min^{-1} . After the injections, the scalp was sutured. The experiments were carried out 3–4 weeks after the injections.

Surgery and shank insertion procedure

The Institutional Animal Care and Use Committee (IACUC) reviewed and approved the protocols for Columbia University's program for the humane care and use of animals and inspects the animal facilities and investigator laboratories. The evaluation of the implanted devices was performed in compliance with the Animal Welfare and Columbia's IACUC regulations under approved IACUC protocol AC-AABE5554 'Development of high-density, implantable recording, imaging and stimulating arrays'. Male mice for this project were

acquired from Jackson Laboratory: transgenics (B6;129S-Gt(ROSA)26Sortm32(CAG-COP4*H134R/EYFP)Hze/J and B6.Cg-Tg(Thy1-COP4/EYFP)9Gfng/J) and WT for the controls and viral injections (C57L/6J). Injected WT mice (8–10 weeks) and transgenic WT mice (6–12 weeks) were deeply anaesthetized with isoflurane with an induction level of 3% and driven by an oxygen flow at the rate of 2 litre per min. The physiological constants were monitored and kept constant during the experiments. First, scalp overlaying the implantation area was removed following a subcutaneous 0.2 ml of bupivacaine injection and a titanium head plate with a circular window of 8 mm diameter in the centre was fixed on the skull with dental cement. Subsequently, a 3×3 mm craniotomy was performed above the somatosensory cortex and the brain was exposed. Dura mater was removed with a fine-tip scalpel. The flexible recording array was laminated on the surface by the injection site. The rigid OLED shank was fixed on the arm of the stereotaxic frame and vertically positioned over the flexible shank. The rigid shank was then carefully inserted inside the brain and the flexible shank was anchored to it with a through hole located at the tip down to 3 mm. The signals from both electrodes were acquired with an Intan RHS2000 electrophysiology amplifier. At the end of the recording session, the animals were sacrificed by cervical dislocation.

Control experiments

We verified the expression of channelrhodopsin by calibrating the response using an external fibre-coupled LED with emission of either 465 or 590 nm (Doric Lenses). A 200 μm , 0.22-numerical-aperture fibre (Thorlabs) fibre was terminated with a 50- μm -diameter cannula (Thorlabs), which was inserted into the mouse cortex. A tungsten electrode was situated next to the cannula end and connected to the Intan RHS recording system for electrophysiology readout. The control experiments were prepared by the same craniotomy as described above.

Data processing

Electrophysiology data were separately analysed for extract spike and LFP information. For the identification of spikes from the raw recording, we first removed the low-frequency LFPs using a digital Butterworth filter between 300 Hz and 4 kHz. Using Kilosort³⁹, we extracted the waveforms and autocorrelograms of spikes that emerge during the stimulation pulses. Units with clean autocorrelograms and minimal interspike-interval (<2 ms) violations were automatically classified as putative single neurons. The recorded data were digitally filtered using a tenth-order Butterworth band-pass filter with corner frequencies at 0.1 Hz and 3 kHz. The LFP bands were analysed with a custom-written MATLAB code to extract the LFP time–frequency information using Gabor wavelet transformations at different frequency bands. The LFP power was calculated within two windows, for a window of 5 s before the application of the stimulation pulses and for the 5 s window during which the stimulation pulses are applied. The Gabor wavelet transform is calculated for integer frequencies between 1 and 50 Hz after applying a Hamming window with a length of 50 ms.

Data availability

The data used in this study are available from the corresponding authors upon reasonable request. Source data are provided with this paper.

Code availability

The custom MATLAB code used in this study to analyse the electrophysiology data is available via GitHub at <https://github.com/klshepard/Electrophysiology-analysis-tools>.

References

1. Lee, C., Lavoie, A., Liu, J., Chen, S. X. & Liu, B. H. Light up the brain: the application of optogenetics in cell-type specific dissection of mouse brain circuits. *Front. Neural Circuits* **14**, 18 (2020).

2. Sun, Z., Schneider, A., Alyahyay, M., Karvat, G. & Diester, I. Effects of optogenetic stimulation of primary somatosensory cortex and its projections to striatum on vibrotactile perception in freely moving rats. *eNeuro* **8**, 1–14 (2021).
3. Jun, J. J. et al. Fully integrated silicon probes for high-density recording of neural activity. *Nature* **551**, 232–236 (2017).
4. Raducanu, B. C. et al. Time multiplexed active neural probe with 1356 parallel recording sites. *Sensors* **17**, 2388 (2017).
5. Uguz, I. & Shepard, K. L. Spatially controlled, bipolar, cortical stimulation with high-capacitance, mechanically flexible subdural surface microelectrode arrays. *Sci. Adv.* **8**, eabq6354 (2022).
6. Deisseroth, K. Optogenetics: 10 years of microbial opsins in neuroscience. *Nat. Neurosci.* **18**, 1213–1225 (2015).
7. Shemesh, O. A. et al. Temporally precise single-cell-resolution optogenetics. *Nat. Neurosci.* **20**, 1796–1806 (2017).
8. Accanto, N. et al. Multiplexed temporally focused light shaping through a gradient index lens for precise in-depth optogenetic photostimulation. *Sci. Rep.* **9**, 7603 (2019).
9. Farah, N., Levinsky, A., Brosh, I., Kahn, I. & Shoham, S. Holographic fiber bundle system for patterned optogenetic activation of large-scale neuronal networks. *Neurophotonics* **2**, 045002 (2015).
10. Segev, E. et al. Patterned photostimulation via visible-wavelength photonic probes for deep brain optogenetics. *Neurophotonics* **4**, 011002 (2016).
11. Moreaux, L. C. et al. Integrated neurophotonics: toward dense volumetric interrogation of brain circuit activity—at depth and in real time. *Neuron* **108**, 66–92 (2020).
12. Yang, Y. et al. Wireless multilateral devices for optogenetic studies of individual and social behaviors. *Nat. Neurosci.* **24**, 1035–1045 (2021).
13. Scharf, R. et al. Depth-specific optogenetic control in vivo with a scalable, high-density μ LED neural probe. *Sci. Rep.* **6**, 28381 (2016).
14. Dadgar, A. et al. Epitaxy of GaN on silicon—impact of symmetry and surface reconstruction. *New J. Phys.* **9**, 389–389 (2007).
15. Templier, F. GaN-based emissive microdisplays: a very promising technology for compact, ultra-high brightness display systems. *J. Soc. Inf. Disp.* **24**, 669–675 (2016).
16. Day, J. et al. III-nitride full-scale high-resolution microdisplays. *Appl. Phys. Lett.* **99**, 031116 (2011).
17. Linghu, C., Zhang, S., Wang, C. & Song, J. Transfer printing techniques for flexible and stretchable inorganic electronics. *npj Flex. Electron.* **2**, 26 (2018).
18. Huang, Y., Hsiang, E.-L., Deng, M.-Y. & Wu, S.-T. Mini-LED, micro-LED and OLED displays: present status and future perspectives. *Light: Sci. Appl.* **9**, 105 (2020).
19. Bae, J. et al. Quantum dot-integrated GaN light-emitting diodes with resolution beyond the retinal limit. *Nat. Commun.* **13**, 1862 (2022).
20. Vöröslakos, M. et al. HectoSTAR μ LED optoelectrodes for large-scale, high-precision in vivo opto-electrophysiology. *Adv. Sci.* **9**, 2105414 (2022).
21. Carreira, J. F. C. et al. Direct integration of micro-LEDs and a SPAD detector on a silicon CMOS chip for data communications and time-of-flight ranging. *Opt. Express* **28**, 6909–6917 (2020).
22. Kim, K. et al. Artifact-free and high-temporal-resolution in vivo opto-electrophysiology with microLED optoelectrodes. *Nat. Commun.* **11**, 2063 (2020).
23. Buckley, A., Underwood, I. & Yates, C. J. The technology and manufacturing of polymer OLED on complementary metal oxide semiconductor (CMOS) microdisplays. in *Organic Light-Emitting Diodes (OLEDs)* 459–511 (Woodhead Publishing, 2013).
24. Maindron, T. et al. Curved OLED microdisplays. *J. Soc. Inf. Disp.* **27**, 723–733 (2019).
25. Murawski, C., Pulver, S. R. & Gather, M. C. Segment-specific optogenetic stimulation in *Drosophila melanogaster* with linear arrays of organic light-emitting diodes. *Nat. Commun.* **11**, 6248 (2020).
26. Kim, D. et al. Ultraflexible organic light-emitting diodes for optogenetic nerve stimulation. *Proc. Natl Acad. Sci. USA* **117**, 21138–21146 (2020).
27. Hillebrandt, S. et al. High brightness, highly directional organic light-emitting diodes as light sources for future light-amplifying prosthetics in the optogenetic management of vision loss. *Adv. Opt. Mater.* **11**, 2200877 (2022).
28. Keum, C. et al. A substrateless, flexible, and water-resistant organic light-emitting diode. *Nat. Commun.* **11**, 6250 (2020).
29. Deng, Y., Keum, C., Hillebrandt, S., Murawski, C. & Gather, M. C. Improving the thermal stability of top-emitting organic light-emitting diodes by modification of the anode interface. *Adv. Opt. Mater.* **9**, 2001642 (2020).
30. Hayashi, K. et al. Suppression of roll-off characteristics of organic light-emitting diodes by narrowing current injection/transport area to 50 nm. *Appl. Phys. Lett.* **106**, 093301 (2015).
31. Leino, A. A., Pulkkinen, A. & Tarvainen, T. ValoMC: a Monte Carlo software and MATLAB toolbox for simulating light transport in biological tissue. *OSA Contin.* **2**, 957–972 (2019).
32. Wu, F. et al. Monolithically integrated μ LEDs on silicon neural probes for high-resolution optogenetic studies in behaving animals. *Neuron* **88**, 1136–1148 (2015).
33. Lin, J. Y. A user’s guide to channelrhodopsin variants: features, limitations and future developments. *Exp. Physiol.* **96**, 19–25 (2011).
34. Marshel, J. H. et al. Cortical layer-specific critical dynamics triggering perception. *Science* **365**, eaaw5202 (2019).
35. Chen, R. et al. Deep brain optogenetics without intracranial surgery. *Nat. Biotechnol.* **39**, 161–164 (2021).
36. Kim, K. et al. GaN-on-Si μ LED optoelectrodes for high-spatiotemporal-accuracy optogenetics in freely behaving animals. In *2016 IEEE International Electron Devices Meeting (IEDM)* 26.5.1–26.5.4 (IEEE, 2016).
37. McAlinden, N. et al. Thermal and optical characterization of micro-LED probes for in vivo optogenetic neural stimulation. *Opt. Lett.* **38**, 992–994 (2013).
38. Stark, E., Koos, T. & Buzsáki, G. Diode probes for spatiotemporal optical control of multiple neurons in freely moving animals. *J. Neurophysiol.* **108**, 349–363 (2012).
39. Csicsvari, J., Hirase, H., Czurrkó, A., Mamiya, A. & Buzsáki, G. Oscillatory coupling of hippocampal pyramidal cells and interneurons in the behaving rat. *J. Neurosci.* **19**, 274–287 (1999).
40. Bansal, H., Gupta, N. & Roy, S. Theoretical analysis of optogenetic spiking with ChRmine, bReaChES and CsChrimson-expressing neurons for retinal prostheses. *J. Neural Eng.* **18**, 0460b8 (2021).
41. Marshel, J. H. et al. Cortical layer-specific critical dynamics triggering perception. *Science* **365**, eaaw5202 (2019).
42. Steriade, M., Nunez, A. & Amzica, F. A novel slow (<1 Hz) oscillation of neocortical neurons in vivo: depolarizing and hyperpolarizing components. *J. Neurosci.* **13**, 3252–3265 (1993).
43. Murawski, C., Fuchs, C., Hofmann, S., Leo, K. & Gather, M. C. Alternative p-doped hole transport material for low operating voltage and high efficiency organic light-emitting diodes. *Appl. Phys. Lett.* **105**, 113303 (2014).
44. Ronzitti, E. et al. Submillisecond optogenetic control of neuronal firing with two-photon holographic photoactivation of chronos. *J. Neurosci.* **37**, 10679–10689 (2017).
45. Sridharan, S. et al. High-performance microbial opsins for spatially and temporally precise perturbations of large neuronal networks. *Neuron* **110**, 1139–1155 (2022).

46. Gong, X. et al. An ultra-sensitive step-function opsin for minimally invasive optogenetic stimulation in mice and macaques. *Neuron* **107**, 38–51 (2020).
 47. Ghosh, A. et al. 62-1: invited paper: directly patterned 2645PPI full color OLED microdisplay for head mounted wearables. *SID Symp. Dig. Tech. Pap.* **47**, 837–840 (2016).
 48. Lee, H. et al. Device characteristics of top-emitting organic light-emitting diodes depending on anode materials for CMOS-based OLED microdisplays. *IEEE Photonics J.* **10**, 8201809 (2018).
 49. Deng, Y. et al. Development of very high luminance p–i–n junction-based blue fluorescent organic light-emitting diodes. *Adv. Opt. Mater.* **8**, 1901721 (2020).
 50. Templier, F. *OLED Microdisplays. OLED Microdisplays: Technology and Applications* (John Wiley & Sons, 2014).
 51. Steude, A., Jahnel, M., Thomschke, M., Schober, M. & Gather, M. C. Controlling the behavior of single live cells with high density arrays of microscopic OLEDs. *Adv. Mater.* **27**, 7657–7661 (2015).
 52. Knowles, M. R. H. Micro-ablation with high power pulsed copper vapor lasers. *Opt. Express* **7**, 50–55 (2000).
 53. Choi, J. et al. A 512-pixel, 51-kHz-frame-rate, dual-shank, lens-less, filter-less single-photon avalanche diode CMOS neural imaging probe. *IEEE J. Solid-State Circuits* **54**, 2957–2968 (2019).
 54. Archer, E. et al. Accurate efficiency measurements of organic light-emitting diodes via angle-resolved spectroscopy. *Adv. Opt. Mater.* **9**, 2000838 (2021).
 55. Yang, W., Carrillo-Reid, L., Bando, Y., Peterka, D. S. & Yuste, R. Simultaneous two-photon imaging and two-photon optogenetics of cortical circuits in three dimensions. *eLife* **7**, e32671 (2018).
 56. Mager, T. et al. High frequency neural spiking and auditory signaling by ultrafast red-shifted optogenetics. *Nat. Commun.* **9**, 1750 (2018).
 57. Yona, G., Meitav, N., Kahn, I. & Shoham, S. Realistic numerical and analytical modeling of light scattering in brain tissue for optogenetic applications. *eNeuro* **3**, e0059–15.2015 (2016).
 58. Kienle, A., Forster, F. K. & Hibst, R. Influence of the phase function on determination of the optical properties of biological tissue by spatially resolved reflectance. *Opt. Lett.* **26**, 1571–1573 (2001).
 59. Pachitariu, M., Steinmetz, N., Kadir, S., Carandini, M. & Kenneth D., H. Kilosort: realtime spike-sorting for extracellular electrophysiology with hundreds of channels. Preprint at *bioRxiv* <https://doi.org/10.1101/061481> (2016).
- C.-K.M. acknowledges funding from the European Commission through a Marie-Sklodowska Curie Individual Fellowship (101029807).

Author contributions

A.J.T., I.U., S.H., C.-K.M., M.C.G. and K.L.S. designed the research. A.J.T. designed, fabricated and packaged the CMOS probe and supporting electronics. S.H., C.-K.M. and C.K. designed, fabricated and characterized the OLEDs on CMOS. A.J.T. and I.U. built the in vivo measurement platform. I.U. designed and performed the neural implantations. I.U. developed the flexible MEA probe and analysed the electrophysiological data. J.C. supported the packaging and design of the CMOS. V.A.-P. and I.U. performed the ChRmine injections. K.D. supplied the ChRmine viral injections. K.L.S. and M.C.G. supervised the research. A.J.T., I.U., S.H., C.-K.M., M.C.G. and K.L.S. wrote the manuscript.

Funding

Open access funding provided by Universität zu Köln.

Competing interests

The authors declare no competing interests.

Additional information

Supplementary information The online version contains supplementary material available at <https://doi.org/10.1038/s41928-023-01013-y>.

Correspondence and requests for materials should be addressed to Malte C. Gather or Kenneth L. Shepard.

Peer review information *Nature Electronics* thanks Yiyuan Yang and the other, anonymous, reviewer(s) for their contribution to the peer review of this work.

Reprints and permissions information is available at www.nature.com/reprints.

Publisher's note Springer Nature remains neutral with regard to jurisdictional claims in published maps and institutional affiliations.

Open Access This article is licensed under a Creative Commons Attribution 4.0 International License, which permits use, sharing, adaptation, distribution and reproduction in any medium or format, as long as you give appropriate credit to the original author(s) and the source, provide a link to the Creative Commons license, and indicate if changes were made. The images or other third party material in this article are included in the article's Creative Commons license, unless indicated otherwise in a credit line to the material. If material is not included in the article's Creative Commons license and your intended use is not permitted by statutory regulation or exceeds the permitted use, you will need to obtain permission directly from the copyright holder. To view a copy of this license, visit <http://creativecommons.org/licenses/by/4.0/>.

© The Author(s) 2023

Acknowledgements

This work was supported in part by the Defense Advanced Research Projects Agency (DARPA) under contract N6600117C4012, by the National Institutes of Health under grant U01NS090596, by the Leverhulme Trust (RPG-2017-231) and by the Alexander von Humboldt Stiftung (Humboldt-Professorship to M.C.G.). This work was performed in part at the Columbia Nano Initiative cleanroom facility, at the CUNY Advanced Science Research Center Nanofabrication Facility, and at the Singh Center for Nanotechnology, part of the National Nanotechnology Coordinated Infrastructure Program, which is supported by the National Science Foundation grant NNCI-2025608.